Unveiling thermal transport properties of defective $\beta-Ga_2O_3$ through machine learning potentials

Yang Su,[1] Jin Yan,[1] Meiyang Yu,[2] Chen Shen,[3,*] Yuhao Fu,[1,†] Tianhang Zhou,[4,‡] and Lijun Zhang[2]

[1]*State Key Laboratory of High Pressure and Superhard Materials, International Center of Computational Method and Software, College of Physics, Jilin University, Changchun 130012, China*

[2]*State Key Laboratory of Integrated Optoelectronics, Key Laboratory of Automobile Materials of MOE, and School of Materials Science and Engineering, Jilin University, Changchun 130012, China*

[3]*Department of Materials and Earth Sciences, Technical University of Darmstadt, Darmstadt, Germany*

[4]*College of Carbon Neutrality Future Technology, China University of Petroleum, Beijing, China*

(Received 22 October 2025; revised 18 February 2026; accepted 16 March 2026; published 9 April 2026)

The intrinsically low thermal conductivity of $\beta-Ga_2O_3$ poses a major challenge for high-power and high-frequency electronic applications. This issue becomes more severe in the presence of defects, which further suppress heat dissipation, exacerbate self-heating, and degrade device performance. In this work, we develop an efficient machine learning potential (MLP) based on a deep neural network model for accurately describing pristine and point-defective $\beta-Ga_2O_3$. Using equilibrium molecular dynamics (EMD) simulations, we quantify the reduction in thermal conductivity induced by intrinsic point defects. Our results demonstrate that Ga interstitials exert the strongest suppression, decreasing the thermal conductivity by 79.5%. Moreover, Ga-related defects generally have a more pronounced impact than O-related defects. This behavior originates from the enhanced vibrations of weakly bonded Ga atoms, increased phonon anharmonicity, and a substantial reduction in the group velocity of low-frequency phonons. These results provide atomic-level insight into thermal transport in defective $\beta-Ga_2O_3$, offering guidance for thermal-management strategies and establishing a general workflow for investigating thermal physics in complex semiconductor materials.

DOI: 10.1103/fdrt-2chf

I. INTRODUCTION

Gallium oxide (Ga_2O_3), particularly the thermodynamically stable β phase, has attracted extensive interest for high-power [1,2], high-temperature electronic devices [3,4] owing to its wide band gap [5] and larger critical electric field [6]. However, the substantial heat generated under high-power operation poses a major challenge to the reliability of $\beta-Ga_2O_3$ devices, especially in the presence of defects. With continued progress in experiments and numerical simulations, the thermal transport properties of $\beta-Ga_2O_3$ have been increasingly understood. Experiments have reported anisotropic thermal conductivity in $\beta-Ga_2O_3$ due to its monoclinic crystal structure [7–10]. On the theory side, thermal conductivity is commonly evaluated using density functional theory (DFT) and molecular dynamics (MD) simulations. Among them, Santia *et al.* [11], Yang *et al.* [12], and Liu *et al.* [13] applied the DFT methods to calculate the thermal conductivity of α, β, and ε-Ga_2O_3, respectively. Nevertheless, because the conventional unit cell of $\beta-Ga_2O_3$ contains 20 atoms, first-principles calculations become prohibitively expensive when large supercells and extensive convergence tests are required.

Recent advances in machine learning [14], particularly deep-learning interatomic potentials [15], provide an effective route to overcome the limitations of empirical force fields. These machine learning potentials (MLPs) have been widely used to predict thermal conductivity in a range of materials, including Si [16], BaAgBi [17], PbTe [18], SnSe [19], and GaN-BAs [20], among others [21–29]. MLP-based simulations typically achieve near DFT accuracy at a computational cost comparable to classical MD. For Ga_2O_3, MLPs combined with equilibrium molecular dynamics (EMD) [30] or homogeneous nonequilibrium molecular dynamics (HNEMD) [31] have been used to evaluate the thermal conductivity of different polymorphs.

Experimentally, unusual point defects in $\beta-Ga_2O_3$ have been directly observed by scanning transmission electron microscopy (STEM) [32]. In addition, the intrinsic structural asymmetry of $\beta-Ga_2O_3$ makes crystals grown by the edge-defined film-fed growth (EFG) method particularly prone to vacancy formation [33]. Although understanding how intrinsic defects affect thermal conductivity is crucial for device thermal management, this issue remains insufficiently explored. Moreover, MLPs that explicitly account for such complex defect configurations have rarely been reported, which hinders reliable large-scale simulations. EMD driven by accurate MLPs can bridge this gap by combining first-principles-level fidelity with MD efficiency. A detailed understanding of thermal transport in defective $\beta-Ga_2O_3$ is

*Contact author: chenshen@tmm.tu-darmstadt.de
†Contact author: fuyuhao@gmail.com
‡Contact author: zhouth@cup.edu.cn

Published by the American Physical Society under the terms of the Creative Commons Attribution 4.0 International license. Further distribution of this work must maintain attribution to the author(s) and the published article's title, journal citation, and DOI.

also essential for improving thermal management strategies and optimizing device packaging.

In this work, we train a deep neural network (DNN) MLP on *ab initio* data of pristine $\beta-Ga_2O_3$ and a set of point-defective supercells. We then use EMD simulations to quantify how different intrinsic point defects suppress the thermal conductivity of $\beta-Ga_2O_3$. Taking into account the high-order phonon interaction, the thermal conductivity of $\beta-Ga_2O_3$ was calculated, and the results were in good agreement with the experimental values. Finally, we combine the MLP with the Boltzmann transport equation (BTE) to analyze the contribution of phonon modes and elucidate the physical origin of the defect-induced reduction in thermal conductivity.

II. METHODS

A. Density functional theory

Density functional theory (DFT) calculations were performed within the Vienna *ab initio* Simulation Package (VASP) code, using PBE generalized gradient approximation exchange-correlation functional [34–36]. For geometry optimization calculations, the energy cutoff for the plane wave expansion is set as 700 eV and a $3 \times 4 \times 3$ grid for Brillouin zone sampling [37], with convergence criteria of energy and force set to 1×10^{-6} eV and 1×10^{-2} eV/Å. The optimized lattice parameters of $\beta-Ga_2O_3$ with 20 atoms are $a = 12.44626$ Å, $b = 3.08559$ Å, and $c = 5.88164$ Å with $\beta = 103.6481^\circ$, which are in good agreement with the experimental results [38]. Using the optimized lattice parameters, a $1 \times 4 \times 2$ supercell of a 20-atoms unit cell was assembled to calculate interatomic force constants (IFCs). The second-order harmonic and third-order anharmonic IFCs were calculated using the finite difference method in the Phonopy [39] and Thirdorder [40] software packages. We considered defects in the construction of the supercell when using *thirdorder.py* to generate defect structures. The presence of defects reduces crystal symmetry, thereby increasing computational cost. However, MLP can effectively address this issue. In this case, the defective system is treated as a defective crystal, rather than a scattering source [41]. Furthermore, we used MLP combined with BTE to analyze thermal transport in defective crystals and rationalize defect-induced reductions in thermal conductivity. The displacement of each atom from its equilibrium position was 0.01 Å. The interactions between atoms up to the 4th nearest neighboring were taken into account for the third-order IFCs calculation, and a $5 \times 17 \times 9$ k-space sampling mesh was used for Brillouin zone sampling at a temperature of 300 K. The *scalebroad* was set as 0.1. The reason for using the 4th nearest neighboring was to facilitate comparison with existing research findings [42,43] and thus verify the reliability of the MLP model. The *ngrid*, *scalebroad,* and nearest neighboring parameter tests were shown in the Supplemental Material (SM), Figs. S1(a)–(c) [44]. The selection of the PBE functional and the setting of simulation parameters were consistent with existing studies [43] to better verify the accuracy of the MLP. It should be clarified that the PBEsol functional demonstrates superior performance compared to the PBE functional in both structural optimization and thermal conductivity calculations [45,46], exhibiting better agreement with experimental results ($a = 12.214$ Å, $b = 3.0371$ Å, and $c = 5.7981$ Å with $\beta = 103.83^\circ$). This work also employed the PBEsol functional for structural optimization ($a = 12.28017$ Å, $b = 3.04829$ Å, and $c = 5.63978$ Å with $\beta = 103.6595^\circ$). Furthermore, this work employed the MLP combined with the BTE method to verify the reliability of MLP in assessing thermal transport properties by comparing it with existing studies. However, it is worth noting that Ruan *et al.* demonstrated the importance of higher-order phonon interactions for thermal transport in $\beta-Ga_2O_3$, which cannot be ignored [45].

For *ab-initio* molecular dynamics (AIMD) and the self-consistent field (SCF) calculations, the energy cutoff was reduced to 700 eV, the $1 \times 1 \times 1$ and $3 \times 4 \times 4$ Monkhorst-Pack k-point mesh to sample the Brillouin zone for $1 \times 3 \times 2$ supercell (with 120 atoms for defect-free $\beta-Ga_2O_3$) were employed, and the convergence criteria of energy was 1×10^{-6} eV and 1×10^{-7} eV, respectively. In this work, for the training data of different systems, only the neutral charge was considered.

B. The construction of a machine learning potential model

The Deep Potential-Smooth Edition (DeePot-SE) was used to train the MLP models [15,47]. The potential energy of each atomic configuration is expressed as the sum of the atomic energies and can be determined from the local environment of each atom. To ensure the translational, rotational, and permutational symmetries of the potential energy surface (PES), the local environment of each atom is created by setting appropriate descriptors. The type of descriptor is set to the smoothed version, which contains radial and angular information in DeepPot-SE. In this work, the radial cutoff (r_c) was chosen to be 9.0 Å, which is enough to capture atoms within the first coordination shell of atom i. The smooth cutoff parameter (r_c) was taken as 0.5 Å. The sizes of the embedding network and fitting network were {25, 50, 100} and {240, 240, 240}, respectively. The MLP model was trained by minimizing the loss function (L), which is defined as the sum of different mean-square errors of neural-network potential prediction in the training processes:

$$L(p_\varepsilon, p_f, p_\xi) = p_\varepsilon \Delta\varepsilon^2 + \frac{p_f}{3N} \sum_i |\Delta F_i|^2 + \frac{p_\xi}{9} \|\Delta\xi\|^2, \quad (1)$$

where $\Delta\varepsilon$, ΔF_i, and $\Delta\xi$ represent the root-mean-square errors (RMSEs) of energy, force, and virial, respectively. N is the total number of atoms in the system. The parameters p_ε, p_f, and p_ξ are adjustable weights for the energy, force, and virial stress, which were set to 0.02, 1000, and 0.8 at the start and 8, 2, and 1 at the end of the training process, respectively. To obtain a convergent training model, 6×10^6 training steps were employed.

C. Molecular dynamics simulations for thermal conductivity calculations

The EMD simulations based on the Green-Kubo method were employed to evaluate the thermal conductivity, which were executed in the Large-scale Atomic/Molecular Massively Parallel Simulator (LAMMPS) [48]. The Green-Kubo

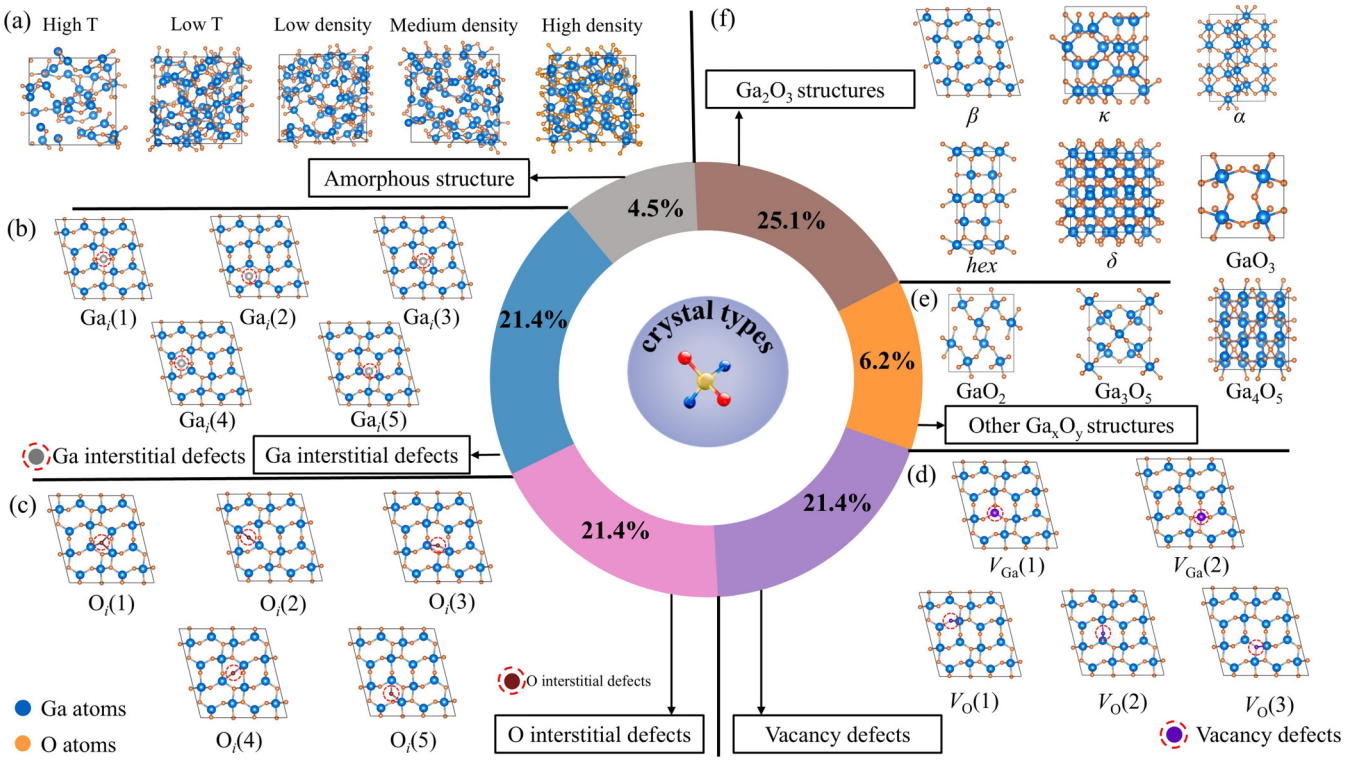


FIG. 1. An overview of dataset configuration, (a) amorphous structures; (b) Ga interstitial defects; (c) O interstitial defects; (d) vacancy defects; (e) Ga_xO_y structures; (f) polytypes of Ga_2O_3 structures.

formula relates the instantaneous fluctuation heat current to the thermal conductivity coefficient based on the autocorrelation function as follows [49]:

$$k_\alpha = \frac{1}{k_B T^2 V} \int_0^{t_0} \langle J_\alpha(0) J_\alpha(t) \rangle dt, \quad \alpha = x,\ y,\ z, \tag{2}$$

where k_B represents the Boltzmann constant, V is the volume of the model, T is the temperature, t_0 is the integral upper limit, which should be infinite theoretically, t represents the correlation time. J_α is the component of heat current J in the α direction, which is expressed as [49]:

$$J = \sum_i \boldsymbol{v}_i E_i + \sum_i \sum_{j \neq i} \boldsymbol{r}_{ij} \left(\frac{\partial U_j}{\partial r_{ij}} \boldsymbol{v}_i \right). \tag{3}$$

Here, v_i and E_i are the velocity and total energy of the atom i, r_{ij} represents the position vector between the two atoms, and U_j is the potential energy of the atom j. For $\beta-Ga_2O_3$, a sufficiently large supercell with 9600 atoms was used for the MD simulation process. In the equilibrium MD calculations of thermal conductivity, to maintain the same defect type as the supercell, the MD defect model was constructed by periodically enlarging the supercell (119 or 121 atoms) containing one defect. The MD simulation box consisted of a $4 \times 5 \times 4$ supercell of vacancy defect structures, giving a total of 9520 or 9680 atoms. Furthermore, to compare the thermal conductivity of random vacancy structures and periodically amplified structures, we established a random structure model for the Ga1 site (V_{Ga}(1)-random). The results show that the average difference in thermal conductivity between the two is approximately 18.6%, as shown in Table SI [44]. Our work primarily focuses on the consequences of ordered defects. The simulations were first performed with the NVT ensemble for 200 ps to ensure that the system was in equilibrium at the simulation temperature. Then, it was switched into the NVE ensemble, and a total of 15 ns heat-flow data were collected. The periodic boundary conditions were applied in all three directions, and the time step is set to 1 fs. A correlation time of 100 ps was sufficient for the thermal conductivity to reach convergence. The average of 15 independent thermal-conductivity simulation values was taken as the final calculation result. The size effect and number of independent simulations of EMD simulations are shown in Figs. S1(c) and (d) [44].

III. RESULTS AND DISCUSSION

A. MLP construction

To obtain a reliable MLP to investigate the thermal transport properties of $\beta-Ga_2O_3$ and the effect of point defects on thermal conductivity, we constructed a comprehensive training dataset based on the structures, energies, and atomic forces of $\beta-Ga_2O_3$-based structures, as shown in Fig. 1. In particular, Zhao *et al.* [37] established a Gaussian approximation potential (GAP) for Ga_2O_3 structures, achieving promising theoretical results. Building on this, we screened and extracted amorphous structures, Ga_xO_y structures, and κ-, γ-, δ-, α-, and hex-Ga_2O_3 structures from this dataset, totaling 1268 configurations. Furthermore, we established datasets for Ga interstitial defects (Ga$_i$), O interstitial defects (O$_i$), and vacancy defects (V_{Ga} and V_O), comprehensively constructing a comprehensive MLP model.

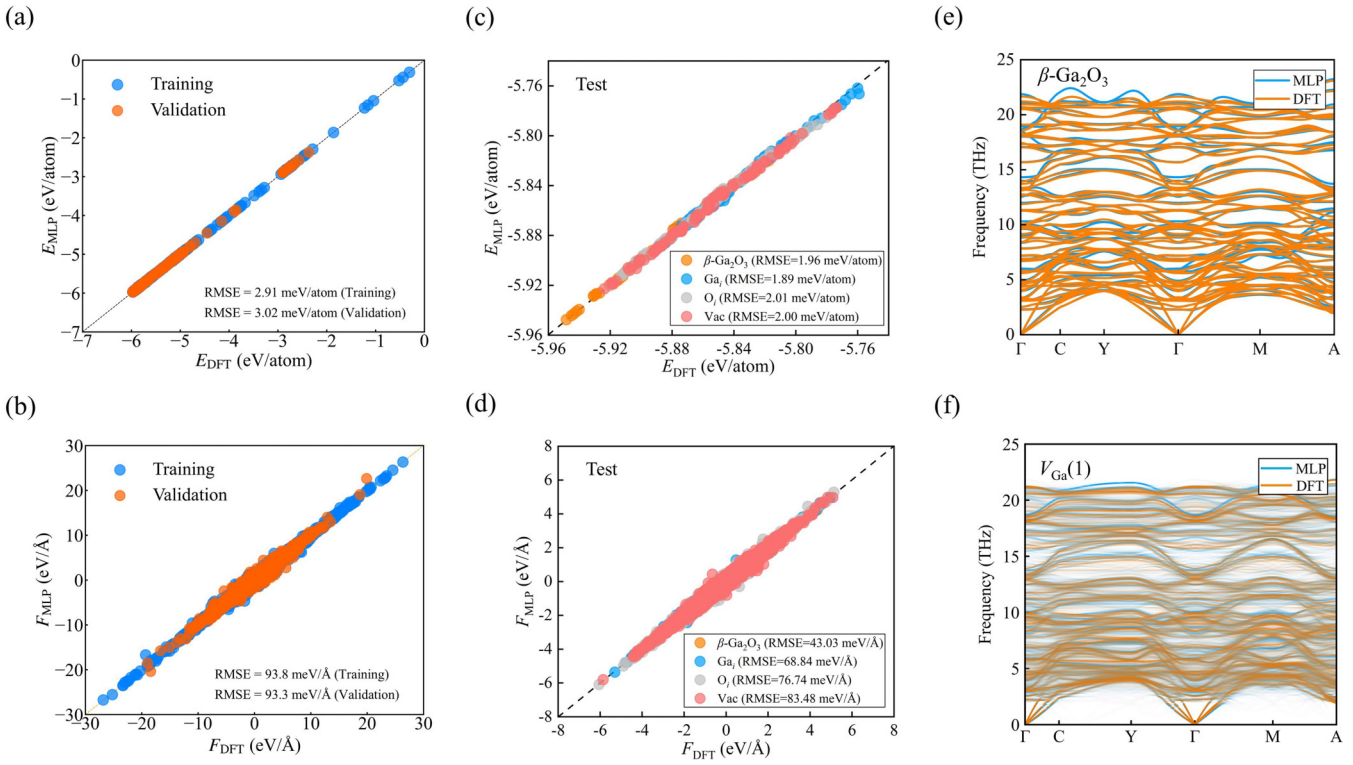


FIG. 2. Comparisons of (a) energy per atom and (b) atomic forces between the MLP and DFT calculations for training and validation datasets, respectively; Comparisons of (c) energy per atom and (d) atomic forces between the MLP and DFT calculations for test datasets; Phonon dispersions of (e) $\beta-Ga_2O_3$ and (f) $V_{Ga}(1)$ from the DFT and MLP calculations. Note that the phonon bands in the Brillouin zone of the supercell are unfolded onto the primitive cell using a band unfolding package [50].

The datasets for the MLP include configurations during the AIMD simulations in the pristine and defective $\beta-Ga_2O_3$ at different temperatures. AIMD simulations were performed in a $(1 \times 3 \times 2)$ supercell (with 120 atoms), considering point defects and a pristine phase at finite temperature, and the configurations of snapshots are randomly collected within the AIMD trajectories. The AIMD simulations in the NVT were performed employing the Nosé-Hoover thermostat for 10 ps with a time step of 1 fs, and the temperature range is from 300 to 900 K. 100 configurations were collected at equal intervals in the MD trajectories of each point defect structure for training, while 200 configurations were taken for the pristine phase. Additionally, 2040 randomly generated $\beta-Ga_2O_3$ and defect configurations are included in the datasets to consider the diverse configurations in the sampling phase space: The lattice constants were randomly varied within 4% and atomic positions are randomly shifted away from the equilibrium position by up to 0.1 Å. We performed active learning configuration collection after one iteration of the MLP, collecting a total of 1550 configurations. The active learning MD runs in the NPT were performed employing the Nosé-Hoover thermostat for 5 ns with a time step of 1 fs, and the temperature range was from 300 to 1000 K. In this work, all configurations were divided into training data and test data in a ratio of 9:1, where the training data was divided into a training dataset and a validation dataset in a ratio of 8:2, and the test dataset was not included in the training dataset or validation dataset. These three sets of data were independent and unique. To evaluate the accuracy of the trained MLP models, the energy and atomic force of structures in the train and validation datasets calculated by DFT and MLP were compared, as shown in Figs. 2(a)–2(b). Generally, the RMSE value of each trained MLP fell within the range of several meV/atom for energy and tens of meV/Å for force, indicating that the training effect is satisfactory. In this work, the RMSEs of energy per atom are 2.910 and 3.015 meV/atom for training and validation datasets, respectively, while the RMSEs of atomic forces are 93.789 and 93.349 meV/Å, respectively. The small RMSE of the training and test datasets indicates that the trained MLP are able to predict DFT-calculated energies and forces of unknown $\beta-Ga_2O_3$ and point defect configurations, and it is suitable for static or dynamic simulations.

Moreover, we evaluated the prediction ability of MLP for the energy and force of different configurations in the test dataset, as shown in Figs. 2(c)–2(d). The results show that the existing MLP still possesses excellent prediction performance for unknown $\beta-Ga_2O_3$ and defect structures. However, the MLPs of $\beta-Ga_2O_3$ system had been reported, but the research had focused on the training of MLPs, while insufficient attention was paid to defect systems. Among them, the GAP potential trained by Zhao *et al.* [37] achieved excellent results and was applied to MD simulations [51]. We evaluated the performance of the GAP potential in defect configurations, but it exhibits significant errors in defect systems, as shown in Fig. S2 [44]. In addition, for theoretical simulations of thermal conductivity, the accuracy of the IFCs obtained by force fitting is also very important. The phonon dispersion of $\beta-Ga_2O_3$ was calculated using DFT and MLP, as shown in Fig. 2(e).

TABLE I. The thermal conductivity ($W\,m^{-1}\,K^{-1}$) of $\beta-Ga_2O_3$ at 300 K predicted by our work and previously reported values.

Method	[100]	[010]	[001]
BTE [11]	16.06	21.54	21.15
BTE [43]	12.7	20.0	17.8
BTE [52]	10.02	23.74	12
BTE [42]	10.63	18.93	13.9
BTE (Bare IFC-3PH) [45]	11.87	20.35	17.35
BTE (Renorm-4PH) [45]	14.84	26.91	19.41
This work (MLP+BTE)	12.85	19.26	14.24
NEP+EMD [53]	9.44	21.46	11.86
NEP+HNEMD [31]	10.3	19.9	12.5
DP+EMD [30]	10.68	20.78	12.61
Experiment [7]	9.5 ± 1.80	22.5 ± 2.50	13.3 ± 1.80
Experiment [8]	10.9 ± 1.0	27.0 ± 2.0	14.7 ± 1.40
Experiment [9]		21.0	
Experiment [10]	13.0 ± 1.0		
This work (MLP+EMD)	9.3 ± 1.25	19.8 ± 2.27	12.5 ± 1.80

In the entire frequency range, the phonon dispersion curve predicted by MLP is consistent with DFT results, indicating that the MLP model can accurately reproduce the potential energy surface of the $\beta-Ga_2O_3$ structure. Similarly, the phonon dispersion of the defect structure was also evaluated, taking $V_{Ga}(1)$ as an example, Fig. 2(f) shows the comparison results of phonon spectrum calculations by MLP and DFT, indicating that MLP can well reproduce the IFCs of the defect structure.

B. Effect of intrinsic interstitial and vacancy defects on the lattice thermal conductivity of $\beta-Ga_2O_3$

After confirming the accuracy of our potential, we employed the MLP combined with BTE methods to calculate the thermal conductivity of the $\beta-Ga_2O_3$, which exhibited minimal deviation from experimental measurements but was slightly higher than the experimental values, as shown in Table I. One reason for this is that the BTE methods truncate the anharmonic force constants to the third order, while molecular dynamics simulations naturally contain higher-order anharmonicities. Moreover, another observation was that there were differences in the thermal conductivity calculated by the BTE methods reported in different literature. It may be attributed to the complexity of the $\beta-Ga_2O_3$ unit-cell and the uncertainty of the convergence of different parameters in such calculations. It is quite challenging to obtain these results accurately. Therefore, we adopted EMD simulations to calculate the thermal conductivity of $\beta-Ga_2O_3$. Figure S3 shows the average integral of the heat flow autocorrelation function along three crystallographic directions at 300 K [44]. The thermal conductivity anisotropy of $\beta-Ga_2O_3$ was observed, with the thermal conductivities in the [100], [010] and [001] directions being $9.27 \pm 1.25\,W\,m^{-1}\,K^{-1}$, $19.79 \pm 2.27\,W\,m^{-1}\,K^{-1}$ and $12.46 \pm 1.80\,W\,m^{-1}\,K^{-1}$, respectively. In Table I, for the $\beta-Ga_2O_3$, our EMD simulation results are consistent with previous experimental results, the HNEMD simulations, and the EMD simulations. The above results show the reliability of the MLP model and the accuracy of the calculation method in this work.

Experimental studies had reported that intrinsic Ga and O interstitial defects were widely distributed in $\beta-Ga_2O_3$ samples [32]. In addition, due to the asymmetry of the $\beta-Ga_2O_3$ lattice structure, Si/Mg-doped $\beta-Ga_2O_3$ crystals prepared by the EFG method were prone to produce vacancy defect structures [33]. Therefore, we considered the effects of different intrinsic interstitial and vacancy point defects on the thermal transport of $\beta-Ga_2O_3$. Using the commonly used EMD simulations, the lattice thermal conductivity of $\beta-Ga_2O_3$ with four different point defects at 300 K was calculated. In Fig. 3(a), at 300 K, the average lattice thermal conductivities of Ga_i, O_i, V_{Ga}, and V_O are 2.81, 5.82, 3.86, and $6.19\,W\,m^{-1}\,K^{-1}$, respectively. Compared with the thermal conductivity of defect-free $\beta-Ga_2O_3$, they were reduced by 79.5%, 57.5%, 71.5% and 55.7%, respectively [Fig. 3(b)]. The results show that any intrinsic point defect can effectively reduce the thermal conductivity of $\beta-Ga_2O_3$, and the effect of Ga interstitial defect was more obvious. Furthermore, we created structures with different defect concentrations to clarify the effect of defect concentration on the thermal conductivity of $\beta-Ga_2O_3$. The results show that the thermal conductivity of $\beta-Ga_2O_3$ with different point defects decreases with the increase of defect concentration, as shown in Fig. S4 [44].

From a dynamic perspective, we analyzed the average single-atom energy. Here, we used the trained MLP model to uniformly calculate the average single-atom energy for perfect phases and defect structures. It is worth noting that the total energy of the system calculated using different MLP models is very similar, but the distribution and magnitude of the atomic site potentials are not unique [54]. In Fig. 3(c), the results show that the average single-atom energy of the defect structure is greater than that of $\beta-Ga_2O_3$, among which the average single-atom energy of the Ga_i structure is the largest. Further, by characterizing the average single-atom energy cloud maps of different structures, it is found that the high-energy atoms in the defects are mainly concentrated around the defects, as shown in Figs. 3(d)–3(h). From Eq. (3), it can be concluded that these high-energy atoms reduce the heat flow value. In addition, the instability of high-energy atoms leads to larger atomic vibrations, which increase phonon scattering in the lattice and thus reduce the lattice thermal conductivity. In Fig. 3(g), the Ga atom vacancy defect causes the movement of the surrounding Ga atoms, thereby increasing the disorder of the structure and reducing the phonon mean free path.

C. Origin of the lower lattice thermal conductivity in $\beta-Ga_2O_3$ with interstitial and vacancy defects

To explore the origin of the low thermal conductivity of different point defects, we used the MLP combined with BTE methods to calculate the thermal transport properties of $\beta-Ga_2O_3$ with different point defect structures [55]. Here, this work only considers third-order phonon interactions to analyze the origin of the decrease in thermal conductivity of defect structures. It should be noted that in the case of defective structures, higher-order phonon interactions may become more important. Considering the possible

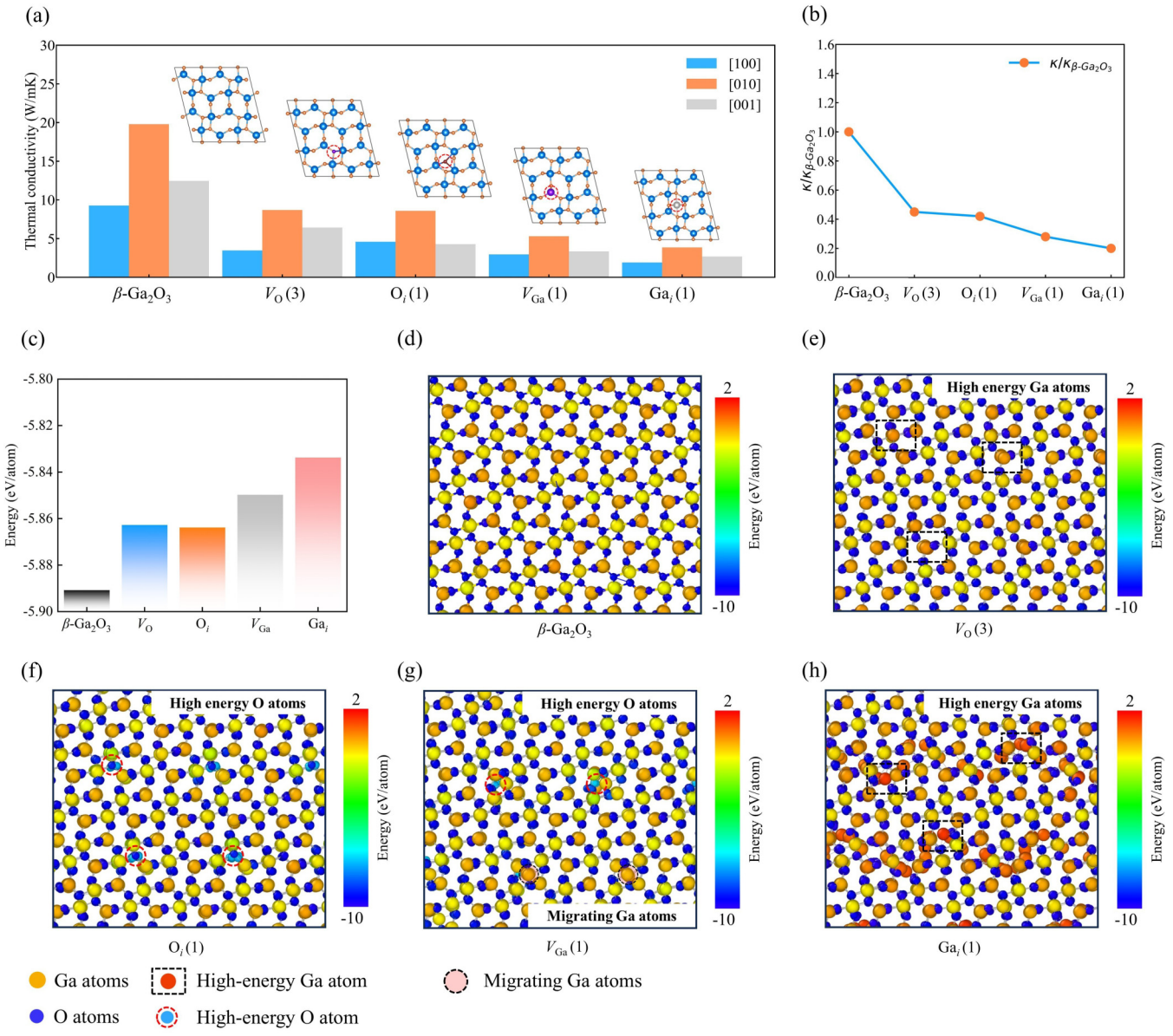


FIG. 3. EMD simulation results: (a) Thermal conductivity of $\beta-Ga_2O_3$ and its point defect structure; (b) Normalized comparison of average thermal conductivity of defect structures; (c) Average single-atom energy of $\beta-Ga_2O_3$ and its point defect structure; (d)–(e) Average single-atom energy cloud diagram of $\beta-Ga_2O_3$ and its point defect structure.

contribution of coherent phonons, we also analyzed coherent transport, as shown in Table SII [44]. The results indicate that for $\beta-Ga_2O_3$, the contribution of coherent transport is relatively small. However, in defective structures, the contribution of coherent transport is significant and cannot be ignored. It can be found that the rate of decrease in average thermal conductivity of the defect structures with temperature is lower than that of the pristine phase, exhibiting weaker temperature dependence, as shown in Fig. 4(a). The phonon dispersions show no imaginary frequency in the entire Brillouin zone, which indicates that the four defect structures are stable. In addition, it can be observed from the phonon dispersions that the acoustic branches of the four structures are flatter compared with those of $\beta-Ga_2O_3$, which means that the propagation speed of phonons is reduced.

To elucidate the mechanisms behind the significant decrease in lattice thermal conductivity of defect structures, we analyzed the scattering rate, phonon group velocity, Grüneisen parameter, and cumulative thermal conductivity. At a given temperature, the lattice thermal conductivity obtained by solving the BTE can be expressed as the sum of the contributions of all the phonon modes (λ) [56]:

$$k_l^{\alpha\beta} = \frac{1}{NV}\sum_{\lambda} C_\lambda \upsilon_\lambda^\alpha \upsilon_\lambda^\beta \tau_\lambda, \tag{4}$$

where N is total number of q points, V is the volume of unit cell, C_λ is the phonon mode heat capacity, $\upsilon_\lambda^\alpha/\upsilon_\lambda^\beta$ represents the phonon group velocity along α and β direction, τ_λ is the phonon lifetime. The calculated heat capacity ratio between the pristine phase and the defect structure is

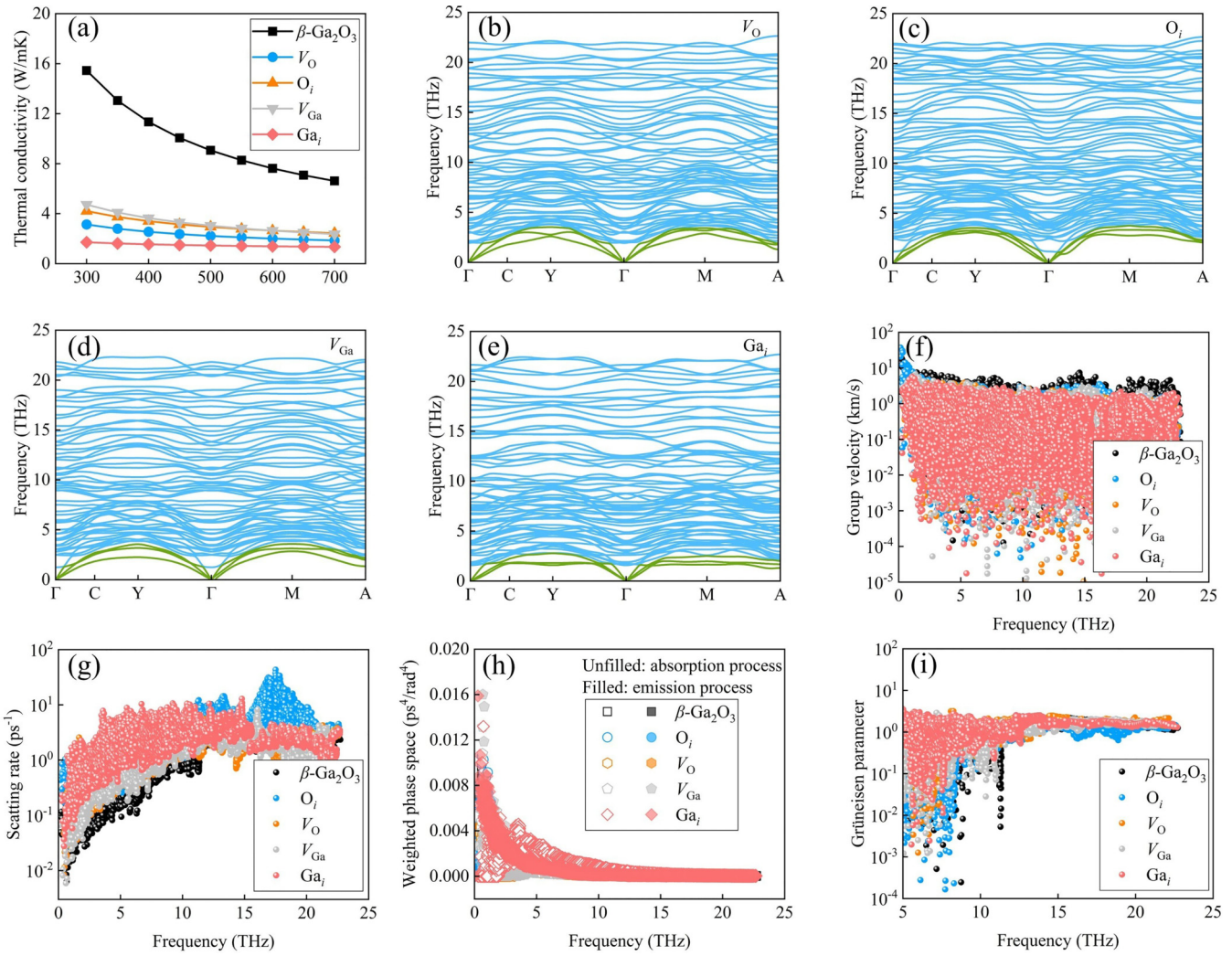


FIG. 4. Calculated results from the BTE: (a) Temperature-dependent thermal conductivity of $\beta-Ga_2O_3$ and its point defect structure (including coherent phonon contribution); (b)–(e) Phonon-dispersion curves of V_O, O_i, V_{Ga} and Ga_i; respectively; Comparison of (f) the group velocity; (j) the scattering rates; (h) the weighted phased space and (i) Grüneisen parameter, respectively.

the smallest at approximately 94.9%, indicating a negligible difference in heat capacity between the two materials (SM, Table SIII) [44]. Moreover, the phonon group velocity of the defect structure is lower than that of $\beta-Ga_2O_3$, but there is no significant decrease [Fig. 4(f)]. Therefore, τ_λ plays a vital role in suppressing the lattice thermal conductivity of the defect structure. Furthermore, the phonon lifetime is primarily determined by the anharmonic scattering rate, and they are quantitatively reciprocal to each other. In Fig. 4(g), it can be found that the scattering rates of defect structures are all higher than those of $\beta-Ga_2O_3$, which means that the probability of three-phonon transitions in defect structures is generally increased, and the number of phonon scattering events is significantly increased. Among them, the Ga_i structure has the highest scattering rate in the acoustic mode, which is also the reason for the largest reduction in its thermal conductivity.

In addition, the weighted phase space is defined as the summation of frequency-dependent components that appear in the calculation of three-phonon transition probabilities $(W \pm \lambda)$ [57,58]:

$$W_\lambda^\pm = \frac{1}{2N}\sum_{\lambda' p''}\left\{\begin{matrix} 2(f_{\lambda'} - f_{\lambda''}) \\ f_{\lambda'} + f_{\lambda''} + 1 \end{matrix}\right\}\frac{\delta(\omega_\lambda \pm \omega_{\lambda'} - \omega_{\lambda''})}{\omega_\lambda \omega_{\lambda'} \omega_{\lambda''}}. \quad (5)$$

In Fig. 4(h), the Ga_i structure exhibits a significant increase in anharmonic scattering rate and weighted scattering phase space during both absorption and emission compared to other defect structures. Specifically, the significant enhancement of low-frequency phonons indicates that these low-frequency phonons may play a dominant role in reducing the lattice thermal conductivity of Ga_i structure, consistent with the cumulative lattice thermal conductivity results (Fig. S5) [44]. Meanwhile, Fig. 4(i) displays the Grüneisen parameter. This parameter reflects the anharmonicity of the lattice. With the introduction of defects, its value increases significantly. This rise indicates enhanced lattice anharmonicity, leading to increased phonon-phonon scattering and consequently reducing the thermal conductivity of the defects.

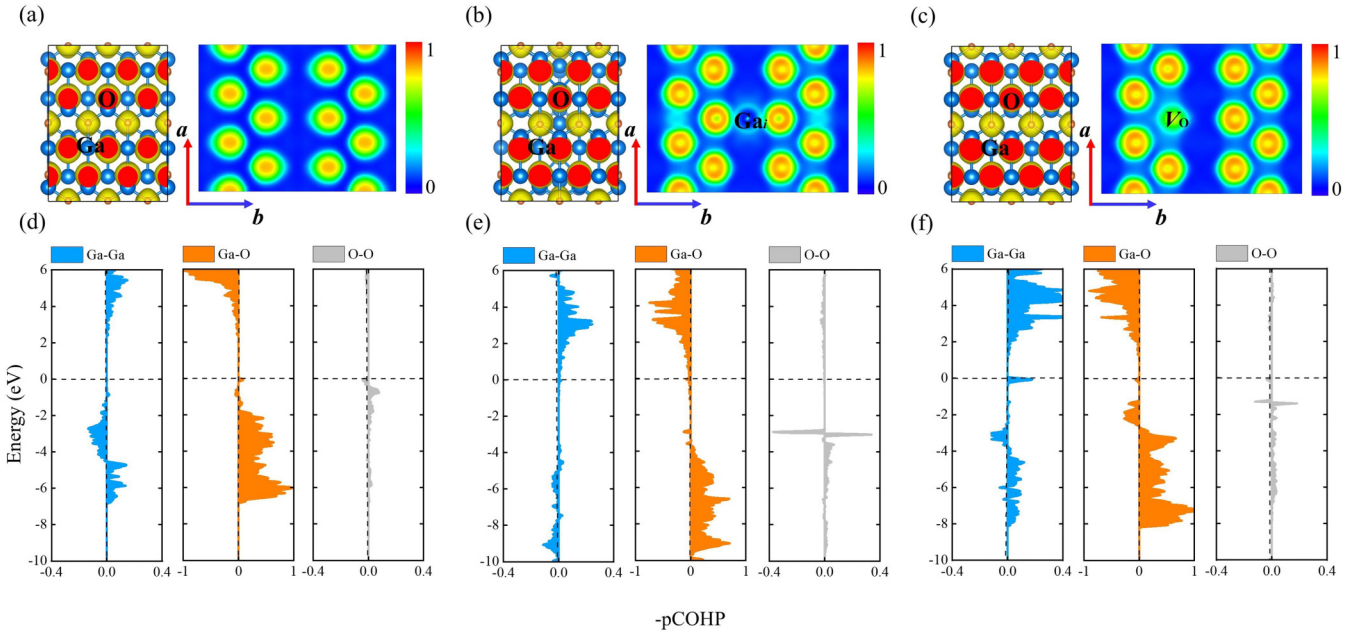


FIG. 5. Isosurfaces of 3D and 2D ELF for (a) $\beta-Ga_2O_3$, (b) Ga_i, and (c) V_O, -pCOHP of various chemical bonds in (d) $\beta-Ga_2O_3$, (e) Ga_i and (f) V_O.

From the electron localization function (ELF) presented in Figs. 5(a)–5(c), the delocalized charge distribution between Ga and O atoms indicates that the Ga-Ga and Ga-O exhibit ionic characteristics. However, the localized charge distribution between O and O atoms implies a covalent bonding behavior. Furthermore, the projected crystal orbital Hamilton population (pCOHP) analysis enables the quantification of bond strength around defects by calculating Hamilton-weighted populations of localized atomic orbitals. Generally, the stronger the interatomic bond strength, the stronger the interatomic coupling, which leads to faster phonon propagation and enhances the lattice thermal conductivity. We have conducted a detailed analysis of the chemical bonding in $\beta-Ga_2O_3$ and its point defect structures, calculated with the LOBSTER package [59]. Positive and negative -pCOHP values represent bonding and antibonding properties, respectively. It can be seen from Figs. 5(d)–5(f) that below the Fermi level, the Ga-Ga and Ga-O bonds have more pronounced antibonding components (the pCOHP of V_{Ga} and O_i, is shown in Fig. S6) [44]. In defect structures, the antibonding states between Ga-Ga and Ga-O bonds are the primary factors weakening bond strength. Furthermore, the integration of pCOHP (ICOHP) below the Fermi level can be used to quantitatively compare different bond strengths (SM, Table SIV) [44]. Therefore, we introduce the parameter Δ to quantify the difference in bond strength between different structures, and Δ is defined as

$$\Delta = [-\mathrm{ICOHP}_{\mathrm{Ga-Ga}}] + [-\mathrm{ICOHP}_{\mathrm{Ga-O}}]. \quad (6)$$

The results show that defects can reduce bond strength, and the weakening effect of Ga_i is the most significant, resulting in the smallest bond strength of Ga_i ($\Delta = 4.33560$) compared with $\beta-Ga_2O_3$ ($\Delta = 6.15472$). Furthermore, weaker chemical bonds lead to significant anharmonicity, which enhances phonon scattering [60].

IV. CONCLUSION

In this work, we developed a comprehensive and accurate machine-learning interatomic potential for pristine and point-defective $\beta-Ga_2O_3$. The predictive capability of the MLP was validated by benchmarking energies, atomic forces, and phonon dispersions against DFT calculations. Using the MLP in conjunction with equilibrium molecular dynamics (EMD), we systematically quantified the impact of intrinsic point defects on the thermal conductivity of $\beta-Ga_2O_3$. All considered defects reduce the thermal conductivity, and Ga interstitials yield the strongest suppression, decreasing thermal conductivity by approximately 79.5%. This reduction is mainly attributed to the pronounced vibrations of weakly bonded Ga atoms, which significantly enhance phonon anharmonicity and suppress the group velocity of low-frequency phonons. Overall, this work demonstrates the usefulness of MLP-enabled simulations for resolving defect effects on thermal transport in complex solids. Our results further suggest that the formation of Ga-related defects should be minimized during material growth and processing to mitigate thermal conductivity degradation and improve heat dissipation in Ga_2O_3 high-power devices.

ACKNOWLEDGMENTS

The authors acknowledge support from the National Natural Science Foundation of China (Grants No. 62125402, No. T2521005, No. 62474081, and No. 22090044). Calculations were performed in part at the high-performance computing center of Jilin University.

DATA AVAILABILITY

The data that support the findings of this article are not publicly available. The data are available from the corresponding authors upon reasonable request.

[1] S. J. Pearton, F. Ren, M. Tadjer, and J. Kim, Perspective: Ga_2O_3 for ultra-high power rectifiers and MOSFETS, J. Appl. Phys. **124**, 220901 (2018).

[2] J. Zhang, P. Dong, K. Dang, Y. Zhang, Q. Yan, H. Xiang, J. Su, Z. Liu, M. Si, J. Gao, M. Kong, H. Zhou, and Y. Hao, Ultra-wide bandgap semiconductor Ga_2O_3 power diodes, Nat. Commun. **13**, 3900 (2022).

[3] J. Zhao, X. Huang, Y. Yin, Y. Liao, H. Mo, Q. Qian, Y. Guo, X. Chen, Z. Zhang, and M. Hua, Two-dimensional gallium oxide monolayer for gas-sensing application, J. Phys. Chem. Lett. **12**, 5813 (2021).

[4] M. Kim, J.-H. Seo, U. Singisetti, and Z. Ma, Recent advances in free-standing single crystalline wide band-gap semiconductors and their applications: GaN, SiC, ZnO, $\beta-Ga_2O_3$, and diamond, J. Mater. Chem. C **5**, 8338 (2017).

[5] J. Y. Tsao, S. Chowdhury, M. A. Hollis, D. Jena, N. M. Johnson, K. A. Jones, R. J. Kaplar, S. Rajan, C. G. Van de Walle, E. Bellotti, C. L. Chua, R. Collazo, M. E. Coltrin, J. A. Cooper, K. R. Evans, S. Graham, T. A. Grotjohn, E. R. Heller, M. Higashiwaki, M. S. Islam, P. W. Juodawlkis, M. A. Khan, A. D. Koehler, J. H. Leach, U. K. Mishra, *et al.*, Ultrawide-bandgap semiconductors: Research opportunities and challenges, Adv. Electron. Mater. **4**, 1600501 (2017).

[6] S. J. Pearton, J. Yang, P. H. Cary, F. Ren, J. Kim, M. J. Tadjer, and M. A. Mastro, A review of Ga_2O_3 materials, processing, and devices, Appl. Phys. Rev. **5**, 011301 (2018).

[7] P. Jiang, X. Qian, X. Li, and R. Yang, Three-dimensional anisotropic thermal conductivity tensor of single crystalline $\beta-Ga_2O_3$, Appl. Phys. Lett. **113**, 232105 (2018).

[8] Z. Guo, A. Verma, X. Wu, F. Sun, A. Hickman, T. Masui, A. Kuramata, M. Higashiwaki, D. Jena, and T. Luo, Anisotropic thermal conductivity in single crystal β-gallium oxide, Appl. Phys. Lett. **106**, 111909 (2015).

[9] Z. Galazka, K. Irmscher, R. Uecker, R. Bertram, M. Pietsch, A. Kwasniewski, M. Naumann, T. Schulz, R. Schewski, D. Klimm, and M. Bickermann, On the bulk $\beta-Ga_2O_3$ single crystals grown by the Czochralski method, J. Cryst. Growth **404**, 184 (2014).

[10] M. Handwerg, R. Mitdank, Z. Galazka, and S. F. Fischer, Temperature-dependent thermal conductivity in Mg-doped and undoped $\beta-Ga_2O_3$ bulk-crystals, Semicond. Sci. Tech. **30**, 024006 (2015).

[11] M. D. Santia, N. Tandon, and J. D. Albrecht, Lattice thermal conductivity in $\beta-Ga_2O_3$ from first principles, Appl. Phys. Lett. **107**, 041907 (2015).

[12] G. Yang, P. R. Romeo, A. Apostoluk, and B. Vilquin, First principles study on the lattice thermal conductivity of α-phase Ga_2O_3, J. Vac. Sci. Technol. A **40**, 052801 (2022).

[13] Q. Liu, Z. Chen, and X. Zhou, Electronic, thermal, and thermoelectric transport properties of ε-Ga_2O_3 from first principles, ACS Omega. **7**, 11643 (2022).

[14] M. Al-Fahdi, C. Lin, C. Shen, H. Zhang, and M. Hu, Rapid prediction of phonon density of states by crystal attention graph neural network and high-throughput screening of candidate substrates for wide bandgap electronic cooling, Mater. Today Phys. **50**, 101632 (2025).

[15] L. Zhang, D. Y. Lin, H. Wang, R. Car, and E. W., Active learning of uniformly accurate interatomic potentials for materials simulation, Phys. Rev. Mater. **3**, 023804 (2019).

[16] R. Li, E. Lee, and T. Luo, A unified deep neural network potential capable of predicting thermal conductivity of silicon in different phases, Mater. Today Phys. **12**, 100181 (2020).

[17] Y. Du, Y. Yao, K. Peng, J. Duan, C. Hao, Y. Tian, W. Duan, L. Yang, P. Lin, and S. Zhang, Impact of vacancy defects on the thermal conductivity of BaAgBi: A comprehensive study using molecular dynamics simulations with neural network potentials, Phys. Chem. Chem. Phys. **26**, 24342 (2024).

[18] M. Qin, X. Zhang, J. Zhu, Y. Yang, Z. Ti, Y. Shen, X. Wang, X. Liu, and Y. Zhang, A machine learning methodology to investigate the lattice thermal conductivity of defected PbTe, J. Mater. Chem. A **11**, 10612 (2023).

[19] P. Zhang, D. Jin, M. Qin, Z. Zhang, Y. Liu, Z. Wang, Z. Lu, R. Xiong, and J. Shi, Effects of four-phonon interaction and vacancy defects on the thermal conductivity of the low-temperature phase of SnSe, Phys. Rev. Appl. **21**, 024043 (2024).

[20] J. Wu, E. Zhou, A. Huang, H. Zhang, M. Hu, and G. Qin, Deep-potential enabled multiscale simulation of gallium nitride devices on boron arsenide cooling substrates, Nat. Commun. **15**, 2540 (2024).

[21] X. Xiang and Y. Zhou, Comparable thermal transport between $Li_{15}Si_4$ and LiSi, Phys. Rev. Mater. **9**, 085401 (2025).

[22] T. Liang, P. Ying, K. Xu, Z. Ye, C. Ling, Z. Fan, and J. Xu, Mechanisms of temperature-dependent thermal transport in amorphous silica from machine-learning molecular dynamics, Phys. Rev. B **108**, 184203 (2023).

[23] L. Zhang, W. Luo, R. Liu, M. Chen, Z. Yan, and K. Cao, Exploring the energy landscape of aluminas through machine learning interatomic potential, Phys. Rev. Mater. **9**, 023801 (2025).

[24] C. Shen, S. Attarian, Y. Zhang, H. Zhang, M. Asta, I. Szlufarska, and D. Morgan, SuperSalt: Equivariant neural network force fields for multicomponent molten salts system, Nat. Commun. **16**, 7280 (2025).

[25] A. Rodriguez, C. Lin, H. Yang, M. A. Fahdi, C. Shen, K. Choudhary, Y. Zhao, J. Hu, B. Cao, H. Zhang, and M. Hu, Million-scale data integrated deep neural network for phonon properties of heuslers spanning the periodic table, npj Comput. Mater. **9**, 20 (2023).

[26] S. Attarian, C. Shen, D. Morgan, and I. Szlufarska, Best practices for fitting machine learning interatomic potentials for molten salts: A case study using $NaCl-MgCl_2$, Comput. Mater. Sci. **246**, 113409 (2025).

[27] R. Jacobs, D. Morgan, S. Attarian, J. Meng, C. Shen, Z. Wu, C. Y. Xie, J. H. Yang, N. Artrith, B. Blaiszik, G. Ceder, K. Choudhary, G. Csanyi, E. D. Cubuk, B. Deng, R. Drautz, X. Fu, J. Godwin, V. Honavar, O. Isayev, A. Johansson, *et al.*, A practical guide to machine learning interatomic potentials - Status and future, Curr. Opin. Solid St. M. **35**, 101214 (2025).

[28] A. Rodriguez, C. Lin, C. Shen, K. Yuan, M. A. Fahdi, X. Zhang, H. Zhang, and M. Hu, Unlocking phonon properties of a large and diverse set of cubic crystals by indirect bottom-up machine learning approach, Commun. Mater. **4**, 61 (2023).

[29] Y. Zhang, C. Shen, T. Long, and H. Zhang, Thermal conductivity of h-BN monolayers using machine learning interatomic potential, J. Phys. Condens Mat. **33**, 105903 (2020).

[30] R. Li, Z. Liu, A. Rohskopf, K. Gordiz, A. Henry, E. Lee, and T. Luo, A deep neural network interatomic potential for studying thermal conductivity of $\beta-Ga_2O_3$, Appl. Phys. Lett. **117**, 152102 (2020).

[31] X. Wang, J. Yang, P. Ying, Z. Fan, J. Zhang, and H. Sun, Dissimilar thermal transport properties in κ-Ga_2O_3 and $\beta-Ga_2O_3$ revealed by homogeneous nonequilibrium molecular dynamics simulations using machine-learned potentials, J. Appl. Phys. **135**, 065104 (2024).

[32] J. M. Johnson, Z. Chen, J. B. Varley, C. M. Jackson, E. Farzana, Z. Zhang, A. R. Arehart, H. L. Huang, A. Genc, S. A. Ringel, C. G. Van de Walle, D. A. Muller, and J. Hwang, Unusual formation of point-defect complexes in the ultrawide-band-gap semiconductor $\beta-Ga_2O_3$, Phys. Rev. X **9**, 041027 (2019).

[33] K. Zhang, Z. Xu, J. Zhao, H. Wang, J. Hao, S. Zhang, H. Cheng, and B. Dong, Temperature-dependent Raman and photoluminescence of $\beta-Ga_2O_3$ doped with shallow donors and deep acceptors impurities, J. Alloy Compd. **881**, 160665 (2021).

[34] K. B. John, P. Perdew, and M. Ernzerhof, Generalized gradient approximation made simple, Phys. Rev. Lett. **77**, 3865 (1996).

[35] G. K. J. Furthmüller, Efficient iterative schemes for *ab initio* total-energy calculations using a plane-wave basis set, Phys. Rev. B **54**, 11169 (1996).

[36] P. E. Blochl, Projector augmented-wave method, Phys. Rev. B **50**, 17953 (1994).

[37] J. Zhao, J. Byggmästar, H. He, K. Nordlund, F. Djurabekova, and M. Hua, Complex Ga_2O_3 polymorphs explored by accurate and general-purpose machine-learning interatomic potentials, npj Comput. Mater. **9**, 159 (2023).

[38] G. S. J. Åhman and J. Albertsson, A reinvestigation of β-gallium oxide, Acta Cryst. **52**, 1336 (1996).

[39] A. Togo and I. Tanaka, First principles phonon calculations in materials science, Scripta Mater. **108**, 1 (2015).

[40] W. Li, J. Carrete, N. A. Katcho, and N. Mingo, ShengBTE: A solver of the Boltzmann transport equation for phonons, Comput. Phys. Commun. **185**, 1747 (2014).

[41] N. A. Katcho, J. Carrete, W. Li, and N. Mingo, Effect of nitrogen and vacancy defects on the thermal conductivity of diamond: An *ab initio* Green's function approach, Phys. Rev. B **90**, 094117 (2014).

[42] J. Yang, Y. Xu, X. Wang, X. Zhang, Y. He, and H. Sun, Lattice thermal conductivity of β-, α- and κ-Ga_2O_3: A first-principles computational study, Appl. Phys. Express **17**, 011001 (2023).

[43] Z. Yan and S. Kumar, Phonon mode contributions to thermal conductivity of pristine and defective $\beta-Ga_2O_3$, Phys. Chem. Chem. Phys. **20**, 29236 (2018).

[44] See Supplemental Material at http://link.aps.org/supplemental/10.1103/fdrt-2chf for parameter testing of thermal conductivity calculated by BTE methods and EMD simulations; comparison of prediction results of GAP potential and DFT on defect structure test datasets; thermal conductivity of $\beta-Ga_2O_3$ along different crystal orientations at 300 K as a function of correlation time using the Green-Kubo methods with the MLP; the trend of thermal conductivity of different defect $\beta-Ga_2O_3$ structure with defect concentration; the cumulative thermal conductivity of $\beta-Ga_2O_3$ and its different defect structure; electron localization function (ELF) and projected crystal orbital Hamiltonian population (pCOHP) and of (a) V_{Ga} and (b) O_i; comparison of thermal conductivity between randomly distributed vacancy structures and supercell periodic amplification structures at 300 K; comparison of coherent thermal conductivity contribution and particle-like channel thermal conductivity contribution at 300 K; calculated phonon mode heat capacity C_λ of $\beta-Ga_2O_3$ and its different defect structure; calculated integration of the pCOHP (ICOHP) of $\beta-Ga_2O_3$ and its different defect structure.

[45] A. Alkandari, Z. Han, Z. Guo, T. E. Beechem, and X. Ruan, Anisotropic anharmonicity dictates the thermal conductivity of $\beta-Ga_2O_3$, Phys. Rev. B **111**, 094308 (2025).

[46] Y. Srivastava, A. G. Gokhale, and A. Jain, Computational uncertainties in the prediction of lattice thermal conductivity of crystalline solids, Phys. Rev. B **112**, 195201 (2025).

[47] H. Wang, L. Zhang, J. Han, and W. E., DeePMD-kit: A deep learning package for many-body potential energy representation and molecular dynamics, Comput. Phys. Commun. **228**, 178 (2018).

[48] S. Plimpton, Fast parallel algorithms for short-range molecular dynamics, J. Comput. Phys. **117**, 1 (1995).

[49] P. K. Schelling, S. R. Phillpot, and P. Keblinski, Comparison of atomic-level simulation methods for computing thermal conductivity, Phys. Rev. B **65**, 144306 (2002).

[50] https://gitlab.abinit.org/xuhe/unfolding.git.

[51] J. Zhang, J. Zhao, J. Chen, and M. Hua, Orientation-dependent atomic-scale mechanism and defect evolution in $\beta-Ga_2O_3$ thin film epitaxial growth, Appl. Phys. Lett. **124**, 022102 (2024).

[52] Y. Chen, L. Peng, Y. Wu, C. Ma, A. Wu, H. Zhang, and Z. Fang, Anomalous temperature-dependent phonon anharmonicity and strain engineering of thermal conductivity in $\beta-Ga_2O_3$, J. Phys. Chem. C **127**, 13356 (2023).

[53] Z. Sun, Z. Qi, K. Liang, X. Sun, Z. Zhang, L. Li, Q. Wang, G. Zhang, G. Wu, and W. Shen, A neuroevolution potential for predicting the thermal conductivity of α, β, and ε-Ga_2O_3, Appl. Phys. Lett. **123**, 192202 (2023).

[54] W. Zhou, B. Tang, Z. Fan, F. Grasselli, S. Baron, and B. Song, Heat transport in superionic materials via machine-learned molecular dynamics, arXiv:2512.04718.

[55] C. Shen, N. Hadaeghi, H. K. Singh, T. Long, L. Fan, G. Qin, and H. Zhang, Two-dimensional buckling structure induces the ultra-low thermal conductivity: A comparative study of the group GaX (X = N, P, As), J. Mater. Chem. C **10**, 1436 (2022).

[56] J. M. Ziman, *Electrons and Phonons: The Theory of Transport Phenomena in Solids* (Oxford University Press, UK, 2007).

[57] W. Li and N. Mingo, Thermal conductivity of fully filled skutterudites: Role of the filler, Phys. Rev. B **89**, 184304 (2014).

[58] W. Li and N. Mingo, Ultralow lattice thermal conductivity of the fully filled skutterudite $YbFe_4Sb_{12}$ due to the flat avoided-crossing filler modes, Phys. Rev. B **91**, 144304 (2015).

[59] S. Maintz, V. L. Deringer, A. L. Tchougréeff, and R. Dronskowski, LOBSTER: A tool to extract chemical bonding from plane-wave based DFT, J. Comput. Chem. **37**, 1030 (2016).

[60] J. Yuan, M. Li, and H. Wang, Intrinsically ultralow lattice thermal conductivity and giant thermoelectric effect in Ag-based intercalated layered crystalline solids, Phys. Rev. B **109**, 235202 (2024).